Scientific Reports

https://doi.org/10.1038/s41598-026-45353-z

Article in Press

Sustainable performance enhancement of a heat recovery ground source heat pump system using field data and machine learning

Received: 6 December 2025

Accepted: 18 March 2026

Published online: 31 March 2026

Cite this article as: Cui Y., Chong W.T., Varman M. *et al.* Sustainable performance enhancement of a heat recovery ground source heat pump system using field data and machine learning. *Sci Rep* (2026). https://doi.org/10.1038/s41598-026-45353-z

Ying Cui, Wen Tong Chong, Mahendra Varman, Xinru Wang, Taocheng Wan, Yun Deng & Song Pan

Sustainable performance enhancement of a heat recovery ground source heat pump system using field data and machine learning

Ying Cui[a, *], Wen Tong Chong[a, b], Mahendra Varman[a, *], Xinru Wang[c], Taocheng Wan[d], Yun Deng[e], Song Pan[d]

[a]Department of Mechanical Engineering, Faculty of Engineering, Universiti Malaya,
Kuala Lumpur 50603, Malaysia

[b]Centre for Energy Sciences, Universiti Malaya, Kuala Lumpur 50603, Malaysia

[c]Department of Building Environment and Energy Application Engineering, Faculty of [1]Mechanical Engineering, Tianjin University of Commerce, Tianjin 300134, China

[d]Beijing Key Laboratory of Green Built Environment and Energy Efficient Technology,
Beijing University of Technology, Beijing 100124, China

[e]Guizhou China Tobacco Industry Co., Ltd. Tongren Cigarette Factory, Tongren 554300, China

[*]Correspondence to: s2138332@siswa-old.um.edu.my, mahendra@um.edu.my

Abstract: To mitigate soil heat accumulation that reduces the energy efficiency of ground source heat pump systems in cooling-dominated regions, a novel heat recovery ground source heat pump (HRGSHP) system is designed and a three-year field test is performed in this paper. The system parallels a conventional condenser and heat recovery condenser within a single heat pump, recovering excess condenser heat to provide 50 °C hot water during summer operation. Results demonstrate that the HRGSHP effectively limits soil temperature rise to □0.45 ℃ while meeting the air conditioning demand. To further enhance efficiency, a multi-objective optimization framework combining a genetic algorithm and backpropagation neural network (GA-BPNN) model with a technique

for order preference by similarity to ideal solution (TOPSIS) is developed. This enables accurate energy performance prediction and optimal operational parameter setpoint determination. The optimized system achieved improvements, with average coefficients of performance for system (COP_s) and heat pump (COP_u) increased by 27% and 11% in winter, respectively, the energy efficiency ratios for system (EER_s) and heat pump (EER_u) increased by 21% and 11% in summer, respectively, and operational costs were reduced by 19%. This work provides experimental evidence and optimization guidelines for implementing HRGSHP systems in building applications.

Keywords: Ground source heat pump, Condensation heat recovery, Field experiments, Energy performance, Optimization, Genetic algorithm

Nomenclature

GSHP	ground source heat pump	$T_{o,g}$	outlet temperature of ground side (°C)
HRGSHP	ground source heat pump with condensation heat recovery	TOPSIS	technique for order preference by similarity to ideal solution
BPNN	back propagation neural network	$T_{i,g}$	inlet temperature of ground source side (°C)
PCC	pearson correlation coefficient	$T_{i,r}$	intlet temperature of heat recovery side (°C)
COP	coefficient of performance	$T_{o,r}$	outlet temperature of heat recovery side (°C)
COP_u	coefficient of heat pump performance	G_u	flow rate of user side (m^3/h)
COP_s	coefficient of system performance	G_g	flow rate of ground side (m^3/h)
EER	energy efficiency ratio	$T_{i,u}$	inlet temperature of user side (°C)
EER_u	energy efficiency ratio of heat pump	$T_{o,u}$	outlet temperature of user side
EER_s	energy efficiency ratio of system	T_s	soil temperature (°C)
MAP	the mean absolute error	t	outdoor temperature (°C)
MAPE	the mean absolute percentage error	d	outdoor humidity (%)

RMSE	the root-mean-square error (%)	GA	genetic algorithm
GHEs	ground heat exchangers	G_r	flow rate of heat recovery side (m^3/h)
HP_s	Heat pump units	IR	improvement rate
ML	machine learning	PIRs	performance improvement rates
P_s	power consumption of system (kW)	P_u	power consumption of HP_s (kW)
T_c	condensing temperature (°C)	T_e	evaporating temperature (°C)

1. Introduction

Building energy consumption accounts for 30%–40% of global final energy consumption[1], with a significant proportion of this energy used for heating, ventilation, and air-conditioning (HVAC) systems[2]. To address this issue, many industrialized nations have invested in renewable energy technologies to reduce their carbon footprints[3]. Ground source heat pump (GSHP) systems exchange heat with stable underground temperatures through ground heat exchangers (GHEs) buried at depths of within 200 m, and then electric-driven heat pumps are used to enhance their heating and cooling regulation capacity[4]. As a result, GSHP systems can operate with relatively stable performance across seasons[5]. They have witnessed substantially increased adoption owing to their high coefficient of performance (COP)[6,7] and potential to reduce energy consumption by up to 40% compared with conventional HVAC systems[8].

Despite these advantages, the long-term operation of GSHP systems in cooling-dominated regions, such as those characterized by hot summers and cold winters (HSCW), often leads to soil thermal imbalance and performance degradation due to the fact that more heat is injected into the ground than extracted[9]. Qian and Wang[10] simulated the changes in soil temperature and COP under four scenarios. For scenario 1, only under a constant 50 kW cooling load, the soil temperature increased by approximately 12.5 °C, and COP decreased by 1.25 after 10 years of operation. In contrast, under a constant 50 kW heating load, the soil temperature decreased by

10.6 °C. To address thermal imbalance, hybrid GSHP (HGSHP) systems commonly integrate cooling towers to reject excess heat to the atmosphere[11–13]. While effective for achieving soil thermal balance, this approach wastes valuable low-grade thermal energy. Specifically, this configuration treats excess heat only as a burden to be rejected, rather than as a recoverable energy resource that can be actively integrated into system operation. In fact, certain special building applications, such as data centers[14], industrial facilities, and archives, during dehumidification cooling cycles for air conditioning, cooling coils often overcool air to remove latent load, followed by electric reheating, leading to further energy waste. This demand for simultaneous cooling and heating presents a prime opportunity for condensing heat recovery.

Previous studies have explored the potential benefits of condensing heat recovery. For instance, Zhao et al.[15] simulated the operation of heating/cooling systems in a Shanghai hotel (TRNSYS) over a 20-year period and found that increasing the heat recovery rate to 53% reduced the annual soil temperature rise from 8.78 °C to 0.34 °C. Zhang et al.[16] found that heat recovery provided 15%–30% energy savings, albeit with a continuous decline in the COP of the system (up to 28% after 20 years) due to independent, dedicated heat recovery units operating year-round. Although this type of system is flexible in layout and operation, it will cause waste of space and investment in intermittent operation conditions of heat recovery.

In addition, achieving and maintaining a high *COP* (>3) and energy efficiency ratio (*EER*) (>3) for such HGSHP systems is challenging, primarily due to the inevitable discrepancies between system design and real-world operation[17]. Achieving optimal performance often requires careful tuning of the operational parameters[18–20]. Conventional performance assessment methods, such as experimental testing and simulations, face practical limitations in large-scale, real-time optimization due to sensor constraints and computational demands[21,22]. Machine learning (ML) techniques provide an effective alternative due to their ability to handle large datasets and capture complex nonlinear behavior. In

particular, for an integrated HRGSHP system with dynamically coupled heat recovery and ground heat exchange processes, data-driven modeling becomes a necessary tool to capture nonlinear interactions and support system-level operational optimization. The random forest (RF)[21], adaptive neural fuzzy inference system (ANFIS)[22], and extreme learning machine (ELM)[23] have been applied to GSHP in previous studies. But most existing applications focus on specific operating conditions or individual GSHP systems, and extending these models to systems involving coupled operating modes remains no easy task. In contrast, the BPNN has been widely demonstrated to be effective in modeling HGSHP[24–26]. However, extending such approaches to HRGSHP systems with frequent switching between cooling and heat recovery introduces additional modeling complexity and places higher demands on model robustness, as parameters such as the weight threshold and the number of inputs of neural networks have a significant impact on the model quality.

While the literature confirms that heat recovery can mitigate soil heat accumulation and utilize waste heat, several gaps remain: (1) increased space requirements due to the separation of heat recovery units from GSHP systems[27], and unclear system structures and thermodynamic principles in existing HRGSHP studies[16,28]; (2) lack of integrated optimization approaches that explicitly consider heat recovery parameters in seasonal GSHP operation; (3) heavy reliance on simulation-based analysis with limited long-term field validation.

To address both the soil thermal imbalance issue and the waste heat recovery opportunity, a novel heat recovery ground source heat pump (HRGSHP) system is proposed here. Based on the principle of Carnot cycle-based heat recovery chillers[29], the HRGSHP system integrates space cooling and heating as well as year-round hot water supply within a single system (see Fig. 1). Its core innovation lies in employing tee valves to arrange two condensers in parallel within a single heat pump unit. This enables the capturing of condenser heat destined for the ground during cooling operations and its repurposing for heating, and/or reheating after dehumidification

cooling, and/or domestic hot water (DHW) supply. The detailed thermodynamic principles and operation modes are seen in Section 2.

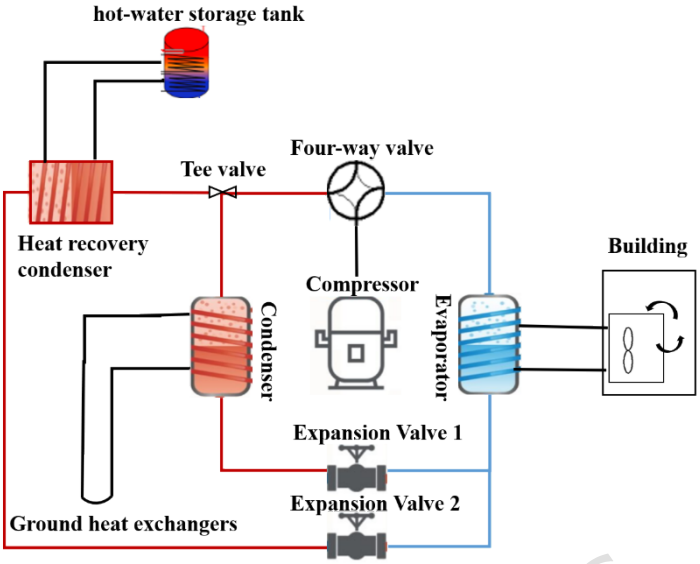

Fig. 1. Schematic of the proposed HRGSHP system.

The main contributions of the present work are the following:

1. System innovation, in which a conventional condenser and a heat recovery condenser are connected in parallel within a single heat pump unit, enabling the direct utilization of recovered condensation heat for air-conditioning hot water supply. This integrated design fundamentally alters the heat rejection pathway of conventional GSHP systems, alleviates soil thermal imbalance, and enables the simultaneous provision of chilled and hot water for air-conditioning purposes. To the authors' knowledge, such an integrated condenser configuration within a single GSHP system has not been previously reported.

2. Field validation, where long-term monitoring of soil temperature and energy performance under real operating conditions in an HSCW climate is conducted, provides rare experimental evidence for the long-term effectiveness of the proposed HRGSHP system.

3. System operational optimization considering multi-parameter interactions. The proposed HRGSHP architecture introduces additional operational parameters and dynamics. This necessitates optimization that explicitly accounts for interactions among multiple

operating parameters. Thus, an optimized BPNN combined with a TOPSIS framework is employed to identify optimal seasonal operating parameter combinations, rather than performing isolated parameter tuning.

4. Quantitative evaluation of performance and cost. The impacts of heat recovery parameters on both COP_s (EER_s) and COP_u (EER_u) for both the system and heat pump (s and u subscripts, respectively), together with associated operating costs, enabling targeted operation set to maximize efficiency.

2 System operation modes and thermodynamic principles

The proposed HRGSHP system integrates a parallel heat recovery condenser into the refrigeration cycle to simultaneously reduce soil heat accumulation and utilize waste heat. By increasing the condensation temperature, this configuration enables the partial or full recovery of the condensation heat. By switching between the four-way and three-way valves, the system can achieve four operating modes. Fig. 2 shows the thermodynamic process of the heat recovery heat pump in the four modes of the system.

1. Cooling Mode (Summer). As seen in Fig. 2 (a), the operation cycle is compressor (1→2), condenser (2→3→4), expansion valve (4→5), and evaporator (5→1). The output is 7 °C chilled water for space cooling.

2. Cooling + Hot Water Mode (Summer). As seen in Fig. 2 (b), there are two operation cycles. For the heat recovery phase, the operation cycle is compressor (1→2), heat recovery condenser (2→3→4), expansion valve (4→5), and evaporator (5→1). The cooling mode, the operation cycle is compressor (1→2), condenser (2→3→6), expansion valve (6→7), and evaporator (7→1). The output is 7.7 °C (state point 8) chilled water and 50 °C hot water. Heat recovery is achieved via tee valve control.

3. Hot Water Mode (Transitional). The operation cycle is the same as the cooling mode (Summer). The output is 50 °C hot water.

4. Heating Mode (Winter). The operation cycle is the same as the cooling mode (Summer). The output is 55 °C hot water for space heating.

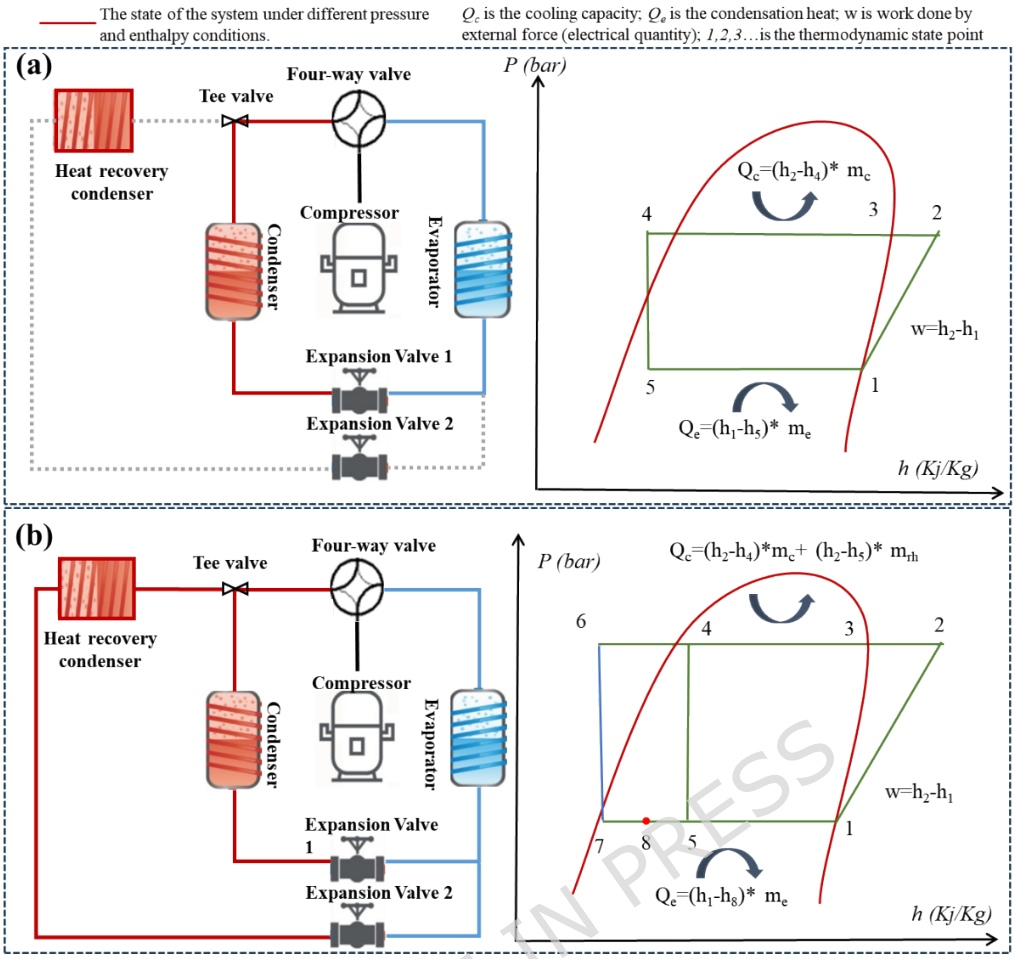

Fig. 2. Schematics of the different modes of the proposed HRGSHP system and corresponding pressure (*P*)–enthalpy (*h*) curves.

3 Methodology

3.1 Field test site description and climate conditions

To assess the performance of the HRGSHP system, field tests were conducted on a demonstration system installed in an industrial building located in Tongren City, Guizhou Province, China. Tongren, which is located in the HSCW region of China, experiences four distinct seasons throughout the year. The climatic conditions and seasonal distribution of the study region, based on long-term meteorological data and Ref. 30[30], are summarized in Table 1. This work primarily focuses on the system operation in winter and summer, as the system is not required during the other two seasons. The onset and duration of the cooling and heating periods are determined based on the local climate conditions as well as the specific temperature and humidity requirements of the building.

Table 1 Climate conditions of Tongren city, Guizhou Province, China.

Item	Value/Description
Average annual precipitation	1208.8mm
Annual temperature	13.5 ℃-17.6 ℃
Highest mean daily temperature in summer	33.0℃, usually in August
Lowest mean daily temperature in winter	3℃, usually in January
Winter	December to late March, last 4 months
Summer	May to September, lasts 4 months
Spring	Late March to April, lasts 2 months
Autumn	October to November, lasts 2 months

Fig. 3 illustrates the operational configuration of the HRGSHP system for different seasons, and the designed parameters of the components based on Chinese standards GB50736-2012 and GB50366-2005 are given in Table 2. A total of 3 heat recovery heat pumps (HR-HPs), which have a cooling capacity of 1713 kW in cooling mode, 1938 kW in cooling and heat recovery mode, and 1705 kW in heating mode, are established in this building for the HRGSHP system. The GHEs are made of high-density polyethylene pipes (HDPE), through which water gets the geothermal energy as a heat source or a heat sink. The GHEs are the closed vertical type (double U-shaped) and have 531 boreholes of 150m in depth. The distance between the boreholes is 5 m. Detailed information on GHEs as seen in Table 2 and their allocation as seen in Fig.4.

In winter, as shown in Fig. 3(a), the system operates in the heating mode, with the GHEs acting as heat sources that transfer heat to the building through the heat recovery heat pumps (HR-HPs). In summer, as shown in Fig. 3(b), the system alternates between the cooling and hot water modes. The transition between these two modes is determined by the water temperature in the hot-water storage tank. As the temperature of the hot-water storage tank falls below 43 °C, the system enters the hot water mode. This transition is driven by the heat recovery condenser of the HR-HPs and the hot-water storage tank. Conversely, as the temperature of the hot-water storage tank exceeds 48 °C, the system enters the cooling mode. In

this mode, the GHEs serve as cold sources, and heat is transferred to the building via the HPs. The cooling/heating output is regulated based on the temperature difference between the supply and return water. If this difference deviates from the set value, the effective working length of the screw compressor is adjusted via the slide valve, which regulates the cooling capacity of the system. The heat recovery heat pumps used in this study are equipped with inverter-driven compressors, allowing continuous modulation of system capacity rather than discrete staged operation. The circulating water pump of the user side is driven by variable-frequency pumps, which are adjusted by a predefined temperature difference, rather than regulated by an online machine-learning-based closed-loop controller. Fig. 5 presents the main components of the HRGSHP system.

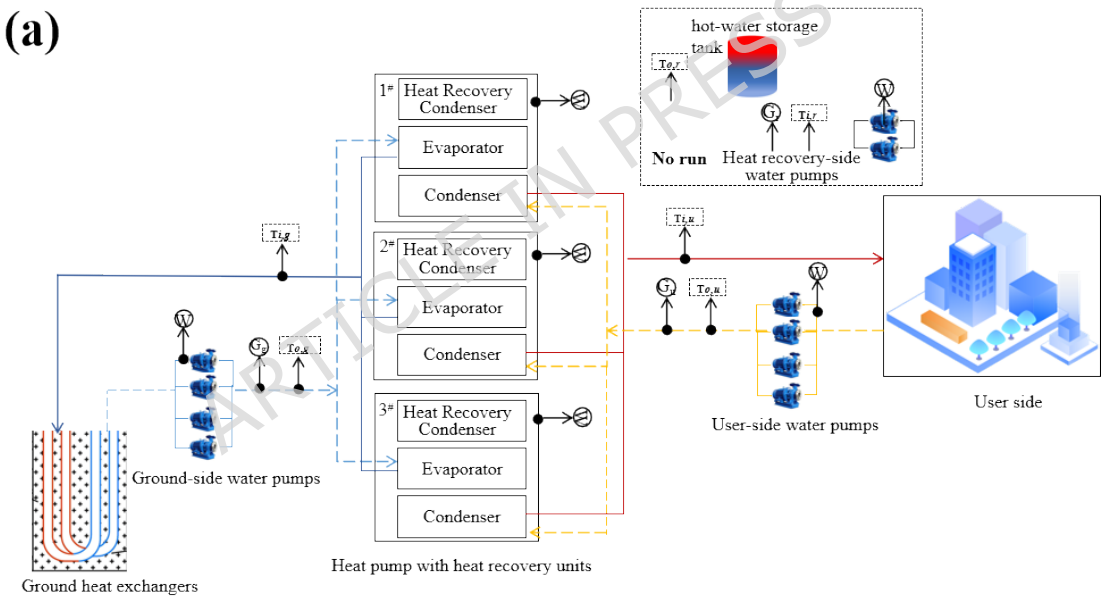

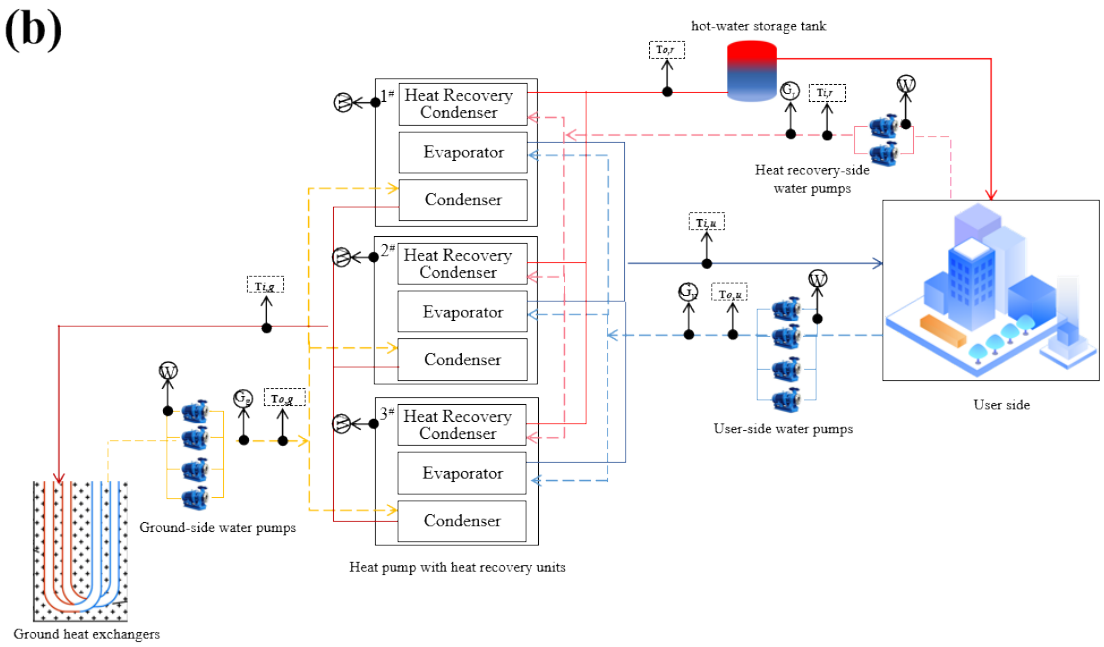

Fig. 3. Process flow diagram of the HRGSHP system for different seasons: (a) winter (December 1 to March 1) and (b) summer (May 1 to September 30).

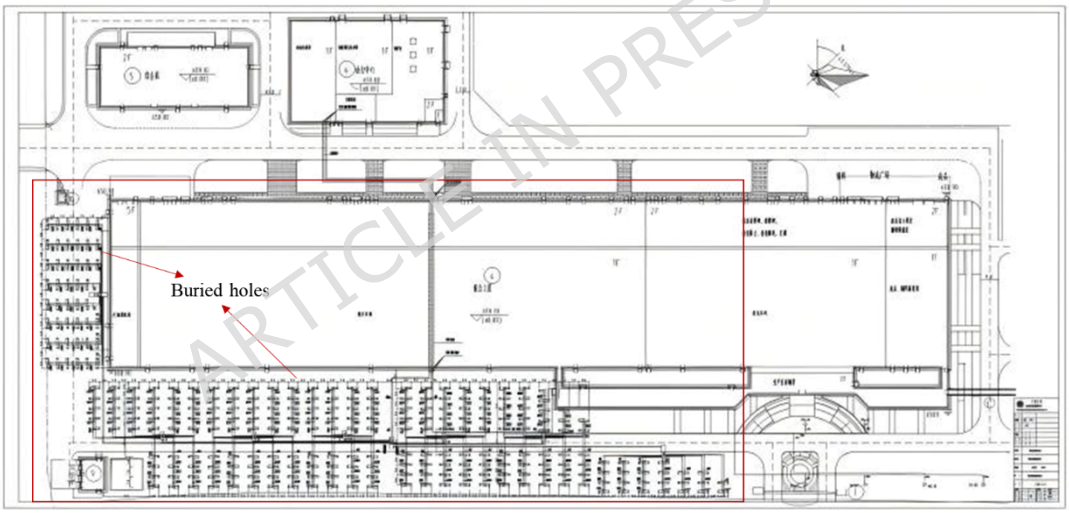

Fig. 4. The distribution of GHEs.

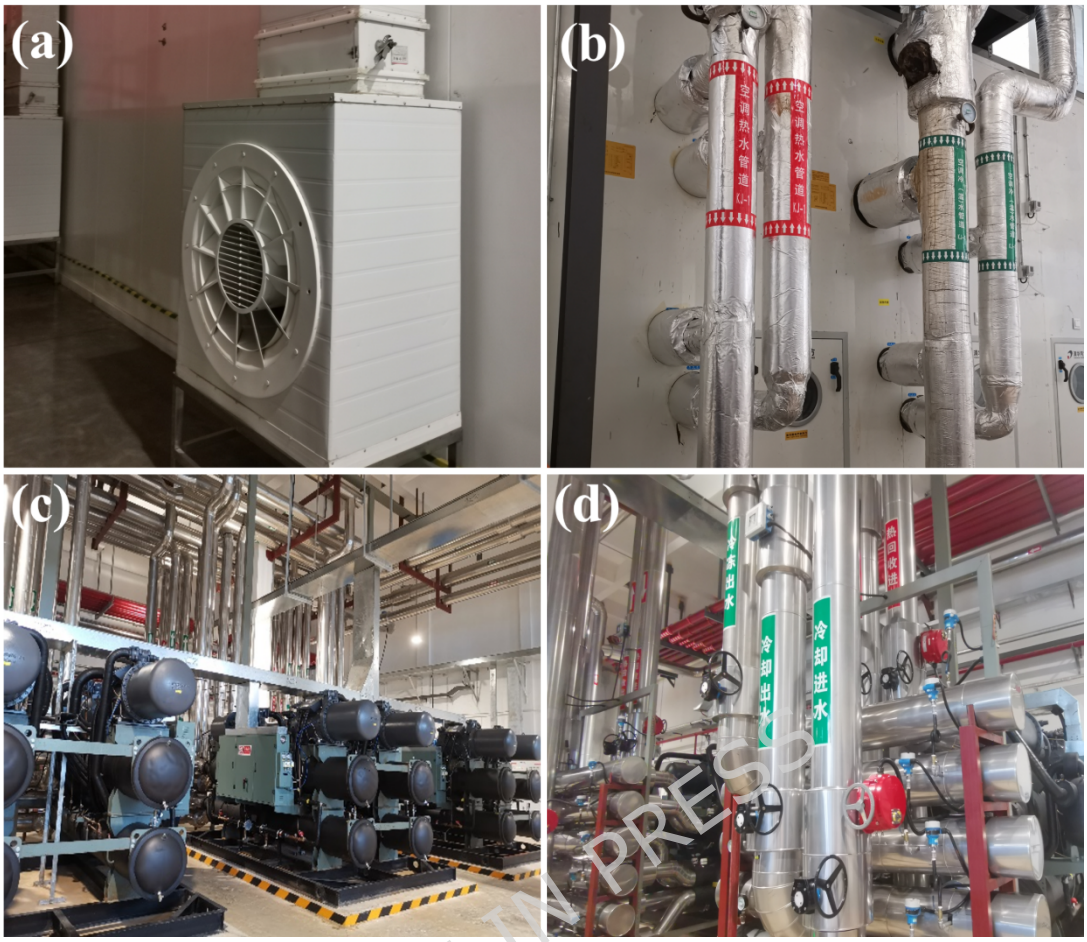

Fig. 5. Photographs of the main components of the HRGSHP system: (a) air conditioning vents, (b) air conditioning unit (provides both hot water and cold water), (c) heat pump units, and (d) heat pump inlet and outlet valves.

Table 2 Designed parameters of the components in the HRGSHP system.

Devices		Information
HR-HPs	Cooling mode	Inlet and outlet water temperature in condenser: 20/ 25 °C; Inlet and outlet water temperature in Evaporator: 12/7 °C; Cooling power: 1713 kW; Electric power: 294 kW; Rated condition COP: 5.82.
	Hot water mode	Inlet and outlet water temperature in condenser: 50/ 55 °C; Inlet and outlet water temperature in Evaporator: 12/7.7 °C; Cooling power: 1938 kW; Electric power: 477 kW; Rated condition COP: 4.06.
	Heating mode	Inlet and outlet water temperature in condenser: 50/ 55 °C; Inlet and outlet water temperature in Evaporator: 10/5 °C;

	Heating power: 1705 kW; Electric power: 475 kW; Rated condition COP: 3.56.
User side water pump	Flow rate: 600 m^3/h; Water head: 39 m H_2O; Electric power: 132 kW.
Ground side water pump	Flow rate: 650 m^3/h; Water head: 60 m H_2O; Electric power: 160 kW.
Heat recovery side water pump	Flow rate: 300 m^3/h; Water head: 20 m H_2O; Electric power: 30 kW.
GHEs circuit	Borehole depth: 150 m; Borehole distance: 5m; Borehole number: 531; GHEs material: high density polyethylene pipes (HDPE); GHEs diameters: DN32; GHEs type: Vertical Double-U;
Hot water storage tank	Volume: 30m^3

3.2 Measurement and evaluation

3.2.1 Data acquisition and instrumentation

To study the actual energy performance of the HRGSHP system during winter and summer, as shown in Fig. 3, the operational parameters were measured at 5-min intervals. A total of 233,856 data points were collected from August 2019 to December 2022, including measurements of the following parameters:

(1) Electricity usage of the interior units (not included in the scope of this study);

(2) Six water temperatures, including the inlet and outlet temperatures of the ground side ($T_{i,g}$ / $T_{o,g}$), user side ($T_{i,u}$ / $T_{o,u}$), and heat recovery side ($T_{i,r}$ / $T_{o,r}$);

(3) Four power consumption parameters (in kWh), including those of the compressors and circulating water pumps;

(4) Three water volumetric flow rates (in m^3/h), including those of the user side (G_u), ground side (G_c), and heat recovery side (G_r);

(5) Soil temperatures (T_s) measured every 10 m in depth inside three temperature-monitoring boreholes located just outside, at the center, and in the periphery of the GHE area;

(6) Outdoor air temperature (t) and humidity (d) obtained from the local meteorological office and integrated into the dataset.

The data were acquired using a long-term monitoring platform.

The sensor loggers were placed at key system locations and calibrated prior to installation to ensure accuracy. The locations of each measurement point are shown in Fig. 3. All measurement data presented in this article were obtained using the instruments listed in Table 3.

Table 3 Measurement instruments and parameters.

Measuring instrument	Time interval	Measured parameter	Accuracy
Temperature sensor	5 minutes	$T_{i,g}, T_{o,g}, T_{i,u}, T_{o,u}, T_{i,r}, T_{o,r}, T_s$	± 0.5 °C
Flow sensor	5 minutes	G_u, G_c, G_r	±1%
Three-phase electric power meter	5 minutes	heat pump electrical power inputs circulating pumps electrical power inputs	± 3%
Temperature and humidity recorder	5 minutes	outdoor dry-bulb temperature outdoor relative humidity	± 0.5 °C

3.2.2 Performance evaluation indicators

The *COP* and *EER*, defined as the ratio of the heat exchange rate to the power consumption, are commonly used to assess the operating efficiency of GSHP systems [31]. These indicators are defined as follows:

$$COP_s/EER_s = \frac{G\rho c_p \Delta t}{3600 P_s} \quad (1)$$

$$COP_u/EER_u = \frac{G\rho c_p \Delta t}{3600 P_u} \quad (2)$$

where ρ is the water density (kg/m^3), c_p is the specific heat capacity at constant pressure (J/(Kg□°C)), D*t*is the water temperature difference on the building side, and G is the water flow rate (m^3/h).

Since the energy performance of a heat pump is influenced by both the evaporation and condensation temperatures, the equations describing the heat pump model contain several nonlinear relationships. Eq. (2) can also be expressed as:

$$COP_u/EER_u = f(T_e, T_c) \quad (3)$$

where T_c and T_e represent the condensation temperature and evaporation temperature, respectively.

3.2.3 Uncertainty analysis

Every measurement involves a certain level of uncertainty. To ensure the accuracy of the research results, an uncertainty analysis of the inputs and outputs is conducted. Compared with other uncertainty propagation methods (such as full-factorial numerical integration, stochastic Galerkin, and discrete projection), the Monte Carlo is very intuitive and easy to implement. Furthermore, this sampling-based technique is generally considered the most dependable method for uncertainty analysis, as it is applicable to a wide range of simulation settings and can handle various probability distributions of input variables, even in cases where the variables are correlated[32,33]. Therefore, in this study, a Monte Carlo probabilistic approach[34] was run with 2000 simulations to estimate the combined relative uncertainty of COP/EER to be on the order of 8.35%. The estimated uncertainty level is within the typical ranges reported in relevant international (ISO) and European (CEN) standards for GSHP system performance measurements[35]. Furthermore, the machine learning models were trained and evaluated using long-term averaged data rather than instantaneous measurements, which further reduces the influence of random sensor noise on model predictions. Thus, the data provided in this study, approximate three years, can support subsequent research.

3.3 Development of the model-based optimization framework

As Eqs. (1)–(3) indicate, the energy performance of the system is highly sensitive to the water temperature parameters. Optimizing these parameters is thus the most effective method to maximize the energy performance of the GSHP system [36,37]. Theoretically, a lower $T_{o,u}$ and a higher $T_{i,g}$ should lead to a lower T_c and a higher T_e, thus improving the energy performance of the heat pumps [38]. In this study, a new optimization method is proposed to optimize T_c and T_e (see Fig. 6). First, the development of a high-accuracy model is essential. In this study, a BPNN integrated with optimization algorithms is employed to construct the predictive model. Commonly used optimization algorithms and their key characteristics are summarized in Table 4. Based on a comprehensive evaluation of

performance, convergence speed, and applicability, the genetic algorithm (GA) is selected to optimize the BPNN parameters. Consequently, a GA–BPNN model is developed based on the experimental data. Four indices, namely EER_s, EER_u, COP_s, and COP_u, are predicted by this model, covering both summer and winter seasons. Next, a correlation analysis is employed to identify the key decision variables affecting these four indices, and a decision matrix is constructed based on the predictions of the GA-BPNN model. Finally, the TOPSIS method is employed to maximize all four performance indicators, thus determining the optimal parameter combination for the system.

Table 4 Commonly used optimization algorithms and their characteristics.

Name	Global Search	Convergence Speed	Principle	Limitation
GA	High	Low	Population-based evolutionary algorithm uses selection, crossover, and mutation.	Parameter tuning is nontrivial
Particle Swarm Optimization (PSO)	Medium–High	Medium	Swarm intelligence, inspired by social behavior, particles update positions using global and personal bests.	Reduced performance in high-dimensional problems
Non-dominated Sorting Genetic Algorithm II (NSGA-II)	High	Low	Pareto-based evolutionary algorithm maintains solution diversity using crowding distance.	High computational cost
Ant Colony Optimization (ACO)	High	Low	Inspired by pheromone-based path finding, probabilistic solution construction.	Limited applicability to continuous problems
Simulated Annealing (SA)	Medium–High	Low	Probabilistic single-solution method, inspired by	Sensitive to the cooling

thermodynamic schedule annealing.

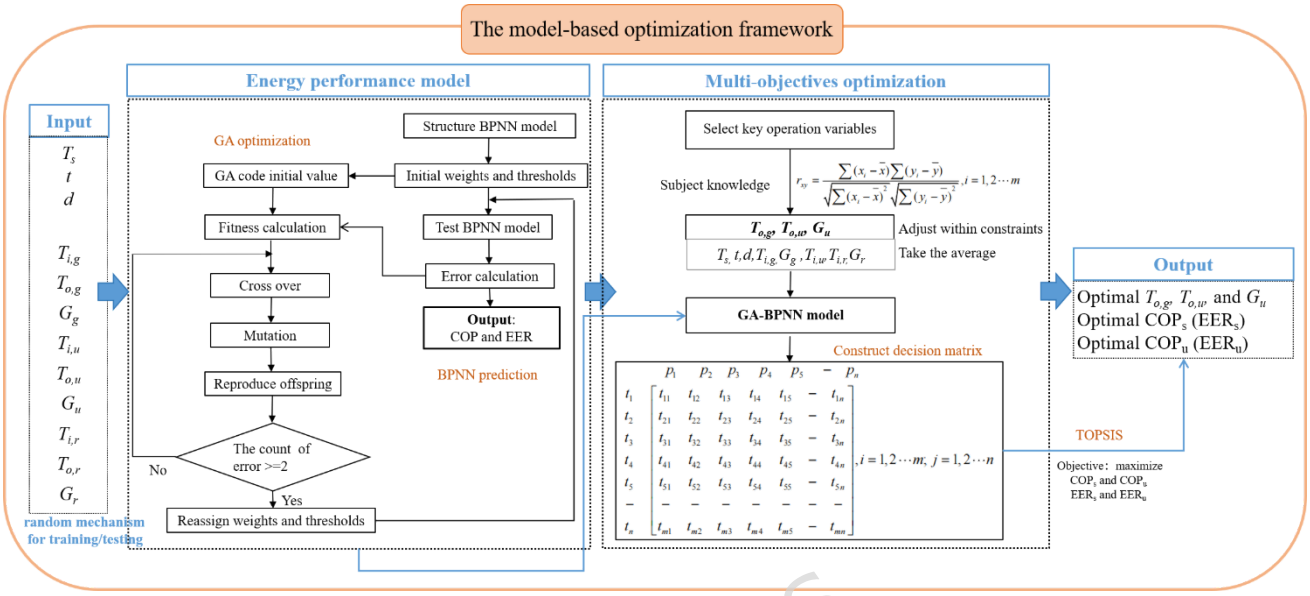

Fig. 6. Optimization process based on the model predictions and the TOPSIS method.

3.3.1 GA-BPNN model construction and training process

The construction of the GA-BPNN model in Fig. 6 can be broken down into the following steps:

Step 1. Determine the network structure according to Eqs. (4-7), including the number of input neurons (corresponding to the selected operational parameters), the number of hidden layers (one hidden layer), and the number of neurons in the hidden layer, which was determined through a trial-and-error process to minimize validation error. The output layer consists of four neurons representing COP_s, COP_u, EER_s, and EER_u. The sigmoid activation function is used in the hidden layer, while a linear activation function is adopted in the output layer.

Step 2. Load and initialize the input dataset, including data selection and training and testing number settings. A random sampling approach was employed to split the original data into training and testing sets, thereby reducing the possibility of introducing bias due to a manual selection of the training set. In addition, to reduce the risk of overfitting, all reported performance metrics were evaluated using the testing data only. Since the dataset

crosses multiple years and operating seasons, the testing set contains samples under diverse thermal and load conditions. This validation strategy allows the predictive performance of the model to be evaluated across different operating regimes, thereby reducing the risk of overfitting.

Step 3. Determine the GA structure according to Eqs. (9-12), including the population size, crossover probability, mutation probability, maximum number of generations for the GA, learning rate, maximum training epochs, and convergence criteria for the BPNN. And initialize the weights and thresholds of BPNN.

Step 4. Run BPNN and calculate the fitness function using Eq. (8)

Step 5. Upgrade BPNN's weights and thresholds calculated by GA. If fitness meets the end condition, go to the next step; If it does not, go back to step 4.

Step 6. Run BPNN using optimal initial weights and thresholds calculated by GA. Update weights and thresholds based on error back propagation.

Step 7. Obtain the optimal prediction model until the network satisfies the end condition.

Specifically, the GA-BPNN model consists of three stages: (i) the neural network construction, (ii) the GA optimization process, and (iii) BPNN training process. The neural network construction procedure is as follows.

For the input layer, the input parameters are described as:

$$X = X_1,\ldots,X_n \tag{4}$$

The output layer, which consists of the COP_s, COP_u, EER_s, and EER_u parameters, is described by the parameter y, as follows:

$$y = S_j\omega_{jk} + b_k \tag{5}$$

where ω_{jk} and b_k are the weights and thresholds between the output layer and the hidden layers, respectively.$S_j$is the transfer function (sigmoid function), which is written as follows:

$$S_j = \frac{1 - e^{H_j}}{1 + e^{H_j}} \tag{6}$$

where H_j is a vector between the input layer and the hidden layer.

This vector can be expressed as follows:

$$H_j = \sum_{i=1}^{n} \omega_{ij} x_i + b_i \quad (7)$$

where ω_{ij} and b_i are the initial weights and thresholds between the input layer and the hidden layer, respectively.

Then, the initial ω_{ij} and b_i were optimized by the GA optimization algorithm. The topology of the BPNN determines the number of optimization parameters required for the GA as well as the code length for the individuals in the GA. The model fitness (F) is calculated in terms of the absolute sum of the differences between the predicted and actual output values, that is:

$$F = a\left(\sum_{i=1}^{n} \mathrm{abs}(y_i - y_i')\right) \quad (8)$$

where n is the number of output nodes, y_i is the output value predicted by the BPNN, y_i' is the actual output value, and a is a model coefficient.

The best weights and thresholds for the BPNN model are identified through sequential selection, crossover, and mutation processes. Individuals exhibiting superior fitness are prioritized and selected to form the subsequent population as follows:

$$P_i = \frac{\frac{b}{F_i}}{\sum_{j=1}^{s} \frac{b}{F_j}} \quad (9)$$

where P_i is the selection probability of individual i, b is a model coefficient, s is the number of individuals in the population, and F_i and $F_j$are the fitness values of individuals i and j, respectively.

In the crossover process, two individuals are selected from the population using the real-number crossover method, allowing new individuals to be generated based on a certain probability as follows:

$$X_{1NEW} = (1 - R_1)X_{1OLD} + X_{2OLD} \quad (10)$$

$$X_{2NEW} = (1 - R_1)X_{2OLD} + X_{1OLD} \quad (11)$$

where X_{1OLD} and X_{2OLD} are the chromosomes X_1 and X_2 before the crossover, respectively, $X_{1NEW}$and X_{2NEW} are the chromosomes X_1

and X_2 after the crossover, respectively, and R_1 is a random number between 0 and 1.

In the mutation process, an individual from the population is randomly selected, and a new individual is generated by applying mutations with a specific frequency as follows:

$$X_{3NEW} = f(x) = \begin{cases} X_{3OLD} + (X_{3OLD} - X_{3MAX}) \cdot R_2 \left(1 - \frac{N}{N_{MAX}}\right) \\ X_{3OLD} + (X_{3MIN} - X_{3OLD}) \cdot R_2 \left(1 - \frac{N}{N_{MAX}}\right) \end{cases} \quad (12)$$

where X_{3NEW} and X_{3OLD} are the chromosome X_3 before and after the mutation, respectively, X_{3MAX} and X_{3MIN} are the boundaries of the chromosome X_3, R_2 and R_3 are random numbers between 0 and 1, N is the current number of iterations, and N_{MAX} is the maximum number of evolutions.

All the above steps were implemented using MATLAB (version 2019). For enhanced model accuracy, an approach mentioned in the literature[39] was adopted to obtain the optimal number of nodes in the model's hidden layer. Specifically, when the input layer is given x nodes, 2x+1 nodes are in the hidden layer. To fine-tune parameters such as the iteration time, population size, crossover probability, and mutation probability, several tests were conducted using the control variable method, leading to the most optimal configuration being selected. Table 5 lists the parameter settings for both the BPNN and GA-BPNN models.

Table 5 Parameter settings for the GA-BPNN model.

BPNN model		GA algorithm	
Parameter	Value	Parameter	Value
Input variables	9(heating)/ 12(cooling)/ 15(transition)	Population size	10
Number of hidden layers	1	Number of iterations	1000
Hidden layer neurons	19(heating) / 25(cooling)/ 31(transitio	Crossover probability	0.4

	n)		
Learning rate	0.05	Mutation probability	0.05
Precision	0.00001		

3.3.2 Model evaluation metrics

Common metrics for assessing the model prediction accuracy include the mean absolute error (*MAE*), mean absolute percentage error (*MAPE*), and root mean square error (*RMSE*). Values closer to 0 indicate greater prediction accuracy [40]. Additionally, the improvement rate (*IR*) is used to express the performance gain of the system after optimization. These metrics are calculated as follows:

$$\mathrm{MAE} = \frac{1}{n}\sum_{i=1}^{n}|y_i - y_i'| \tag{13}$$

$$\mathrm{MAPE} = \frac{1}{n}\sum_{i=1}^{n}\frac{|y_i - y_i'|}{y_i} \times 100\% \tag{14}$$

$$\mathrm{RMSE} = \sqrt{\frac{1}{n}\sum_{i=1}^{n}(y_i - y_i')^2} \tag{15}$$

where n is the number of output nodes, y_i is the actual output value, and y_i' is the predicted output value.

$$\mathrm{IR} = \frac{E' - E}{E} \tag{16}$$

where E' and E are the values after and before optimization, respectively.

3.3.3 Multi-objective optimization using GA-BPNN and TOPSIS

To operate the HRGSHP system efficiently, the optimal combination of the operational parameters should be identified, that is, COP_s (EER_s) and COP_u (EER_u) should be simultaneously maximized. First, the key operational parameters that affect the performance indicators for both summer and winter are selected as decision parameters for the multi-objective optimization, using the Pearson correlation coefficient (*PCC*) and expert knowledge. Table 3 presents the range of values for the decision variables. Next, using the validated GA-BPNN model, target values for different combinations of decision parameters are calculated to yield a solution set for the multi-objective optimization. Finally, to identify

the optimal solution (i.e., the best combination of operational parameters), the TOPSIS method is employed. The multi-objective optimization procedure and the TOPSIS process comprise the following steps:

Step 1: Selecting key operational variables based on the *PCC*

The *PCC* is a measure of the linear relationship between two random variables (real-valued vectors). The *PCC*, here denoted as r_{xy}, is defined as follows [41]:

$$r_{xy}=\frac{\sum(x_i-\bar{x})\sum(y_i-\bar{y})}{\sqrt{\sum(x_i-\bar{x})^2}\sqrt{\sum(y_i-\bar{y})^2}},i=1,2L\ m \tag{17}$$

where $\bar{x}=\frac{1}{n}\sum_{i=1}^{m}x_i$ denotes the mean of x, and $\bar{y}=\frac{1}{n}\sum_{i=1}^{m}y_i$ denotes the mean of y. The coefficient r_{xy} ranges from -1 to 1, and it is invariant to linear transformations of either variable. The closer the value of $|r_{xy}|$ is to 1, the stronger the linear relationship between the two variables [42].

Step 2: Constructing the performance matrix

The elements t_{ij} of the performance matrix are formed by the decision variables p_j ($T_{o,g}$, $T_{o,u}$, $T_{o,r}$, and G_u) varying with the outdoor temperature $t_i$and the corresponding COP_s (EER_s) and COP_u (EER_u). The performance matrix is as follows:

$$\begin{array}{c} \\ t_1 \\ t_2 \\ t_3 \\ t_4 \\ t_5 \\ - \\ t_n \end{array}\begin{array}{c} \begin{array}{ccccccc} p_1 & p_2 & p_3 & p_4 & p_5 & - & p_n \end{array} \\ \begin{bmatrix} t_{11} & t_{12} & t_{13} & t_{14} & t_{15} & - & t_{1n} \\ t_{21} & t_{22} & t_{23} & t_{24} & t_{25} & - & t_{2n} \\ t_{31} & t_{32} & t_{33} & t_{34} & t_{35} & - & t_{3n} \\ t_{41} & t_{42} & t_{43} & t_{44} & t_{45} & - & t_{4n} \\ t_{51} & t_{52} & t_{53} & t_{54} & t_{55} & - & t_{5n} \\ - & - & - & - & - & - & - \\ t_{m1} & t_{m2} & t_{m3} & t_{m4} & t_{m5} & - & t_{mn} \end{bmatrix} \end{array},i=1,2L\ m,j=1,2L\ n \tag{18}$$

Step 3: TOPSIS process

Step 3-1: Normalizing the performance matrix

$$d_{ij}=\frac{t_{ij}}{\sum_{i=1}^{m}t_{ij}},i=1,2L\ m,j=1,2L\ ,n \tag{19}$$

Step 3-2: Calculating the entropy weight

According to Shannon's entropy theory, attributes with a lower dispersion are assigned lower weights to represent their reduced

importance in the overall evaluation process[43].

The entropy value for jth indicator is calculated as:

$$F_j = -K\sum_{i=1}^{m} d_{ij}\ln d_{ij},\ K=\frac{1}{\ln m} \tag{20}$$

Subsequently, based on the entropy value from Eq. (20), the weight for jth indicator is obtained as follows:

$$w_j = \frac{g_j}{\sum_{j=1}^{n} g_j},\ g_j = 1 - F_j \tag{21}$$

where $0 \leqslant w_j \leqslant 1,\ \sum_{j=1}^{n} g_j = 1$.

Step 3-3: Normalizing the weighted decision matrix.

$$u_{ij} = w_j d_{ij},\ i = 1,2,\ldots,m;\ j = 1,2,\ldots,n \tag{22}$$

Step 6: Obtaining the positive ideal points (PISs) and negative ideal points (NISs)

$$r_j = B^+ = \{f_1^+(x), f_2^+(x), \ldots, f_j^+(x), \ldots, f_m^+(x)\} = \{(\max_i f_{ij}(x) \mid j \in J_1), (\min_i f_{ij}(x) \mid j \in J_2), \mid i = 1,2,\ldots,m\} \tag{23}$$

$$h_j = B^- = \{f_1^-(x), f_2^-(x), \ldots, f_j^-(x), \ldots, f_m^-(x)\} = \{(\min_i f_{ij}(x) \mid j \in J_1), (\max_i f_{ij}(x) \mid j \in J_2), \mid i = 1,2,\ldots,m\} \tag{24}$$

where f_m^+ and f_m^- are the r_j and h_j of the i^{th} criterion, respectively, J_1 is the benefit criterion, and J_2 is the cost criterion.

Step 3-4: Calculating the distance between the PISs and NISs for each possible operation

$$d_i^+ = \sqrt{\sum_{j=1}^{n} [f_{ij}(x) - f_j^+(x)]^2},\ j = 1,2,\ldots,n \tag{25}$$

$$d_i^- = \sqrt{\sum_{j=1}^{n} [f_{ij}(x) - f_j^-(x)]^2},\ j = 1,2,\ldots,n \tag{26}$$

Step 3-5: Calculating the rank indexes (rank similarities) of the ideal solution

$$R_i^* = \frac{d_i^-}{d_i^- + d_i^+},\ i = 1,2,\ldots,m \tag{27}$$

where R_i^* is the rank index of the i^{th} possible operation.

4 Results

4.1 Measured system energy performance and soil temperature response

The efficiency of both the refrigeration cycle and the overall HRGSHP system is closely related to T_c and T_e. Since T_c and T_e are influenced by the inlet water temperatures of the condenser and evaporator, the water temperature dynamics and energy efficiency of the HRGSHP system in the different operating modes were analyzed.

4.1.1 Water temperature dynamics

Figure 7 illustrates the temporal variations in water temperatures on the user side, ground side, and heat recovery side during summer and winter operation. As shown in Fig. 7(a), an inverse trend is observed between the user side and ground side temperatures during summer, which is primarily driven by variations in cooling demand and heat rejection intensity. In early summer, when the space cooling load is relatively low, the user side water temperature remains comparatively high, while the heat transferred to the ground is limited, resulting in a lower ground-side temperature. As the cooling demand increases, the system rejects more heat to the ground loop, leading to a gradual reduction in the user side outlet temperature and a rise in the ground side temperature. During peak cooling periods, the user side intlet temperature decreases to approximately 8 °C due to the intensified cooling load, whereas the ground-side outlet temperature increases to about 21–22 °C, indicating significant heat accumulation in the ground. Meanwhile, the heat recovery side temperature exhibits a similar increasing trend to that of the ground side, reaching its maximum during periods of high cooling demand. In contrast, during winter operation (Fig. 7(b)), an opposite thermal behavior is observed. With increasing heating demand, the user side water temperature rises, while the ground side temperature decreases as more heat is extracted from the ground.

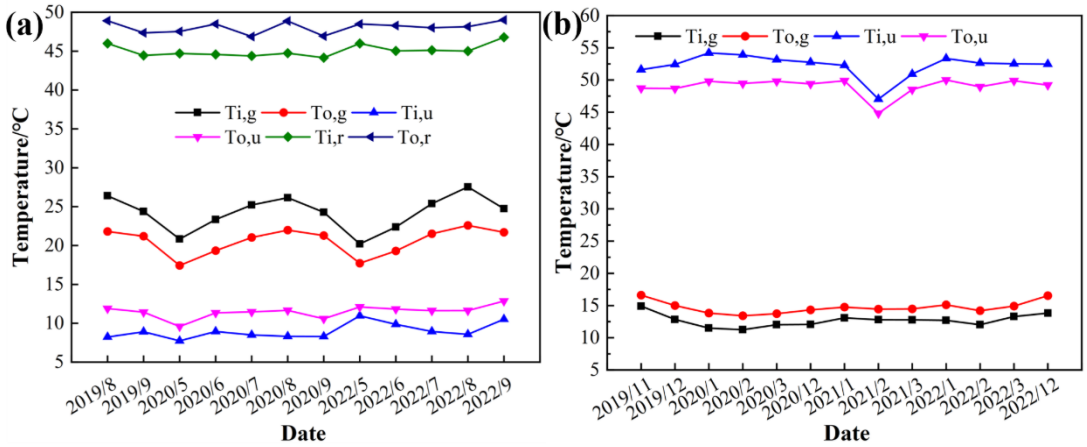

Fig. 7. Monthly water temperature variation for the ground side, user side, and heat recovery side in (a) summer and (b) winter.

4.1.2 Water distribution system efficiency

The efficiency of the water distribution systems on both the user side and the ground side is critical of overall system performance and therefore deserves careful evaluation. Figure 8 presents the temporal evolution of the temperature difference (ΔT) across the user side, ground side, and heat recovery side loops. Owing to the use of constant-speed pumps in the ground-side and heat recovery-side circuits, the corresponding ΔT values exhibit relatively small temporal fluctuations. In contrast, the user-side loop, which is equipped with a variable-speed pump, shows pronounced ΔT variations.

Despite a design temperature difference of 5 °C, the measured ΔT values in all loops are consistently lower. During the summer operation (Fig. 8(a)), the average ΔT values are approximately 3 °C for both the ground-side and heat recovery side loops, while the user side ΔT remains around 2 °C. A similar deviation from the design condition is observed in winter (Fig. 8(b)), where the average ground side ΔT is 2.07 °C, compared with 3.23 °C on the user side.

These results indicate that the flow rates in all loops are excessively high, leading to reduced temperature differentials, hydraulic inefficiency, and unnecessary pump energy consumption. Moreover, the user side flow rate directly influences indoor cooling performance and evaporator heat transfer, whereas the ground side flow rate influences condenser heat rejection performance[38]. Consequently, appropriate flow rate optimization is essential for

improving both the thermal and energetic performance of the HRGSHP system.

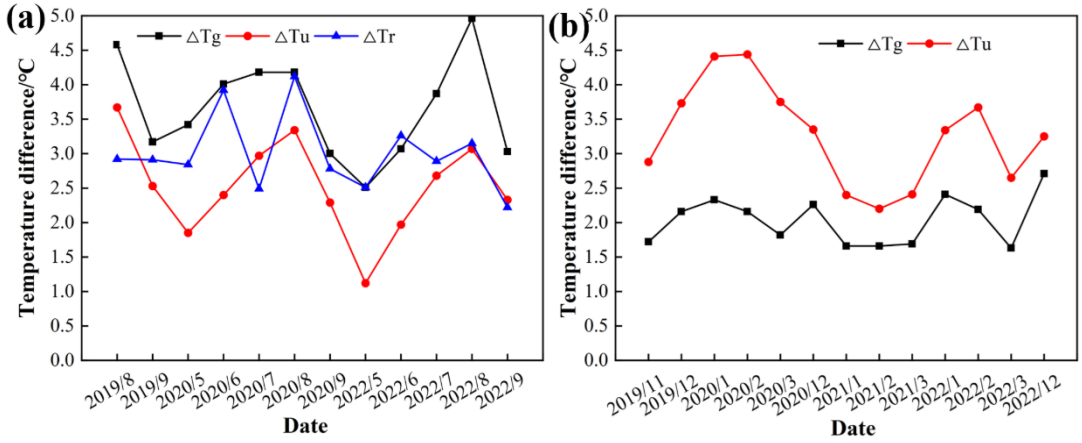

Fig. 8. Monthly water temperature difference variation for the ground side, user side, and heat recovery side in (a) summer and (b) winter.

4.1.3 Seasonal energy performance comparison

Fig. 9(a) presents the annual average *COP* and *EER* values of the HRGSHP system from 2019 to 2022. From 2019 to 2021, both EER_s and EER_u show a gradual decline, decreasing from 3.10 to 2.81 and from 4.72 to 4.16, respectively. A similar downward trend is observed for COP_s and COP_u over the same period. This reduction in efficiency can be primarily attributed to the combined effects of small user side temperature differences (as shown in Fig. 8) and the gradual increase in ground temperature (Fig. 9(b)). The relatively small temperature difference indicates prolonged part-load operation, during which pumping power consumption and frequent compressor cycling increase system losses. Meanwhile, the progressive ground temperature rise reduces heat rejection effectiveness during cooling operation, further contributing to performance degradation. In contrast, a slight rebound in COP_s and COP_u is observed in 2022 following the previous declining trend. Since no structural modifications or control strategy adjustments were implemented during the monitoring period, the observed increase is attributed to variations in operating and thermal conditions. As shown in Fig. 8(b), the user side temperature differences in 2022 is larger than that in 2021, indicating higher load ratios and operating conditions closer to full-load performance. The relatively low load ratio in 2021 was likely associated with reduced

building occupancy during the COVID-19 pandemic period (2020–2021), which decreased heating demand. In contrast, the higher load demand in 2022 enabled more stable and continuous compressor operation with reduced cycling losses, thereby improving system efficiency. In addition, the accumulated increase in ground temperature, while detrimental to long-term cooling performance, temporarily enhances heating-side evaporation temperatures in 2022. This effectively reduced the compressor temperature lift (T_c - T_e), providing a thermodynamic boost to the COP. The combined influence of these two factors contributed to the modest COP rebound observed in 2022, reflecting the nonlinear interaction between ground thermal conditions and operating load characteristics. Notably, the EER_u and EER_s values for 2022 are not reported due to incomplete and discontinuous cooling-season monitoring data, which were excluded to ensure the reliability and representativeness of annual performance indicators.

According to the Chinese national standard GB/T 50801–2013[44], the performance of the GSHP system is classified into three levels, with Level 3 representing the minimum acceptable performance. The corresponding threshold values are 3.0 for EER_s and 2.6 for COP_s. Over the entire monitoring period, the average COP_s and EER_s are 2.86 and 3.10, respectively, indicating that the system performance only marginally satisfies the lowest classification level. Additionally, while the nominal heat pump performance values for COP_u and EER_u are 3.56 and 5.82, respectively, the corresponding actual values are 3.65 and 4.42, respectively, indicating a significant performance gap, particularly under cooling conditions. This can be primarily attributed to real-world operating characteristics of the HRGSHP system. In practice, the system frequently operates under partial-load conditions and switches between cooling and heat recovery modes, especially during the summer season. In addition, long-term ground thermal imbalance leads to elevated ground loop temperatures, which degrade heat transfer performance. These factors collectively increase auxiliary energy consumption and reduce the actual COP_u and EER_u, with a more significant impact on

cooling performance.

It should be noted that the reported soil temperature values in Fig. 9(b) represent long-term averages measured at a depth of 150 m, which effectively reduce the influence of short-term climatic variability and interannual weather fluctuations. Under these conditions, the observed soil temperature increase of 0.45 °C over three years is considerably lower than the 1.63 °C increase over two years reported for a conventional GSHP system under comparable operating conditions in the literature[15]. Although the comparison is based on literature data rather than systems operated under identical boundary conditions, the results provide support that the proposed HRGSHP system is effective in mitigating soil heat accumulation in cooling-dominated regions.

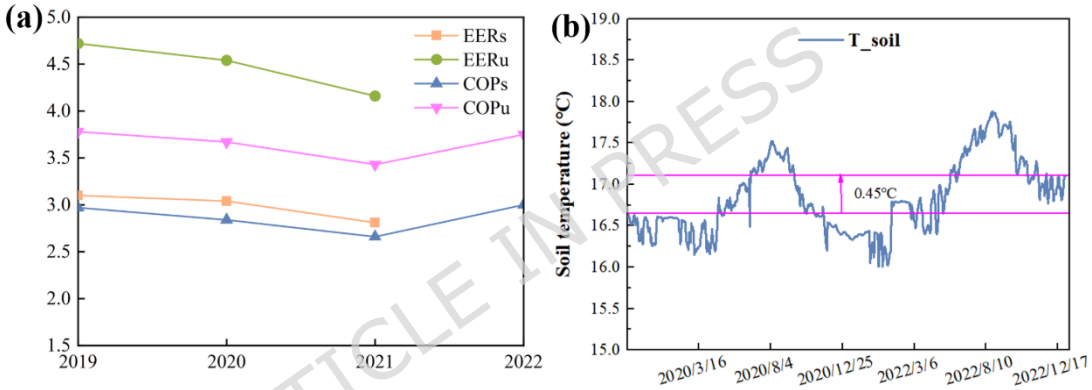

Fig. 9. Observed variations in the *COP*, *EER*, and soil temperature for the HRGSHP system from 2019 to 2022: (a) yearly average *COP* and *EER* variations and (b) daily average soil temperature variation.

These results highlight inefficiencies under real operating conditions, underscoring the need for dynamic optimization strategies[17]. ML-based approaches offer a promising solution by enabling accurate efficiency predictions and operational parameter optimization under varying conditions using historical data. Unlike physics-based models, ML-based approaches require fewer explicit input parameters, however, their accuracy depends critically on data quality and model architecture[45]. Furthermore, operational complexity poses further modeling challenges. In summer, frequent switching between heat recovery and cooling modes (driven by simultaneous heating and cooling demands) introduces data

heterogeneity and instability. The optimization methodology proposed in the subsequent sections addresses these challenges.

4.2 Prediction model performance and comparative analysis

4.2.1 GA-BPNN prediction model

As described in the methodology section, the core of the proposed optimization method is the development of a model that describes the actual energy performance of the HRGSHP system. The *COP* and *EER* prediction models were established based on Eqs. (4)–(12) using the measured data presented in Section 4.1. Figs. 10 and 11 compare the predicted and observed *COP* and *EER* values. The model predictions are in excellent agreement with the measured values, with relative errors typically below 10% for each season. Specifically, the average relative errors for COP_s, COP_u, EER_s, and EER_u are 8.00%, 6.99%, 7.68%, and 5.60%, respectively. Notably, the *EER* predictions are more accurate than the *COP* predictions. As discussed in Section 4.1, the frequent switching of the HRGSHP system between different operating modes during summer introduces data fluctuations and irregularities, which inherently reduce the model prediction fidelity. Nonetheless, the proposed GA-BPNN demonstrates strong robustness in predicting *EER*.

The predictions for COP_u and EER_u are more accurate than those for COP_s and EER_s. This is likely due to the fact that COP_u and EER_u primarily reflect the heat pump performance and compressor loading, while COP_s and EER_s capture the overall system efficiency, which is influenced by interactions between heat pumps, chilled water pumps, and cooling water pumps. These factors introduce nonlinearities that result in less robust predictions for COP_s and EER_s. Crucially, such interactions are often more difficult to model accurately, reinforcing the need for data-driven approaches. Overall, these results validate the capacity of the GA-BPNN model to accurately predict the energy performance of the HRGSHP system during complex, multi-modal operation.

In addition, the prediction accuracy varies seasonally, with the model performance being generally better during the heating season than the cooling season (see Table 6). This is attributed to the lower

operational complexity in the former case: The heating mode employs nine parameters, while the cooling mode requires 12 parameters to manage simultaneous heating/cooling demands.

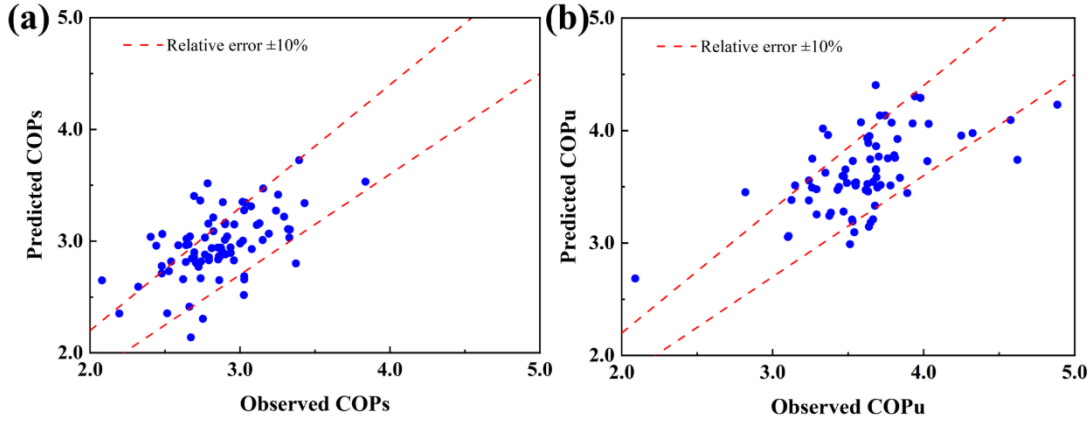

Fig. 10. Comparison between the observed and GA-BPNN-predicted *COP* values.

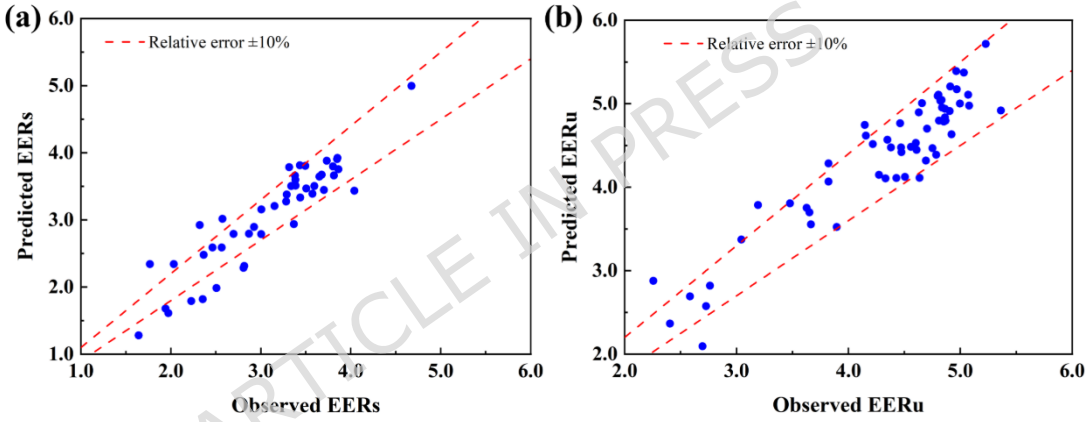

Fig. 11. Comparison between the observed and GA-BPNN-predicted *EER* values.

4.2.2 Model robustness comparison between GA-BPNN and BPNN

To show the advantages of the proposed GA-BPNN model for predicting the performance of the HRGSHP system, a conventional BPNN model using identical training and testing sets was developed. Model accuracy was quantified using the *MAE*, *MAPE*, and *RMSE* (see Eqs. (13)–(15)). Fig. 12 and Table 6 present the comparative results, while Fig. 12 illustrates the *MAPE* distribution across 10 test runs. In all cases, the GA-BPNN model outperforms the BPNN model, achieving consistently lower *MAPE* values for both *COP* and *EER*. Table 6 provides the average optimal values for the three metrics. The best performance for the BPNN model is observed for COP_s

during the heating season under a single heating operation mode, with corresponding *MAE*, *MAPE*, and *RMSE* values of 0.2764, 0.0966, and 0.2597, respectively; however, these values are all higher than those achieved by the GA-BPNN model, indicating the inferior performance of the BPNN model. As shown in Table 6, the optimal performance for the BPNN model is observed for COP_s during the heating season under a single-operation mode, with *MAE* = 0.2764, *MAPE* = 9.66%, and *RMSE* = 0.2597. Notably, all these errors are higher than those obtained using the GA-BPNN model, confirming the superior predictive capability of the latter.

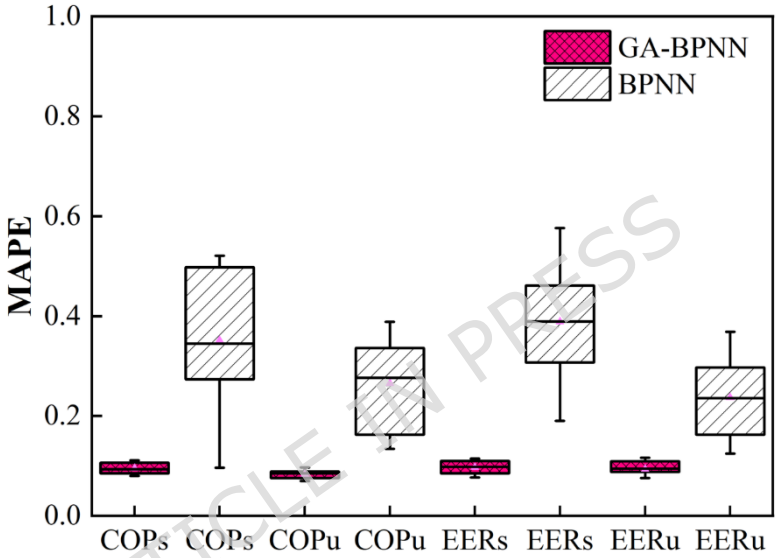

Fig. 12. Comparison of the *MAPE* values obtained from the GA-BPNN and BPNN models.

Table 6 Optimal values of the model performance metrics.

Operation seasons	Performance indicators	GA-BPNN models			BPNN models		
		MAE	MAPE	RMSE	MAE	MAPE	RMSE
Winter	COP_s	0.2288	0.0800	0.1912	1.0058	0.3517	0.6246
	COP_u	0.2523	0.0699	0.2637	1.1112	0.3076	0.7096
Summer	EER_s	0.2379	0.0768	0.1875	0.9453	0.3053	0.9308
	EER_u	0.2434	0.0560	0.1794	1.0724	0.2468	0.8236

The performance improvement rates (*PIRs*, Eq. (16)) further confirm the superiority of the GA-BPNN model (Fig. 13). The *MAE*

and *MAPE PIRs* are comparable (about 77%) for the *COP*/*EER* predictions. On the other hand, the *RMSE* improvements vary: 60% for COP_s and COP_u, and 79% for EER_s and EER_u. These gains can be attributed to the capacity of the GA-BPNN model to overcome a crucial BPNN limitation, that is, trapping in local minima during training. By contrast, by employing a genetic algorithm to optimize the network weights and thresholds, the GA-BPNN model attains globally optimal solutions, reducing prediction bias and enhancing model stability. While data quality remains vital, particularly given seasonal operational shifts and parameter fluctuations, the GA-BPNN model demonstrates exceptional robustness in handling these complexities.

In summary, the GA-BPNN model provides a reliable, highly accurate framework for predicting the energy performance of dynamically operated HRGSHP systems, with significant potential for guiding optimization in real-world applications.

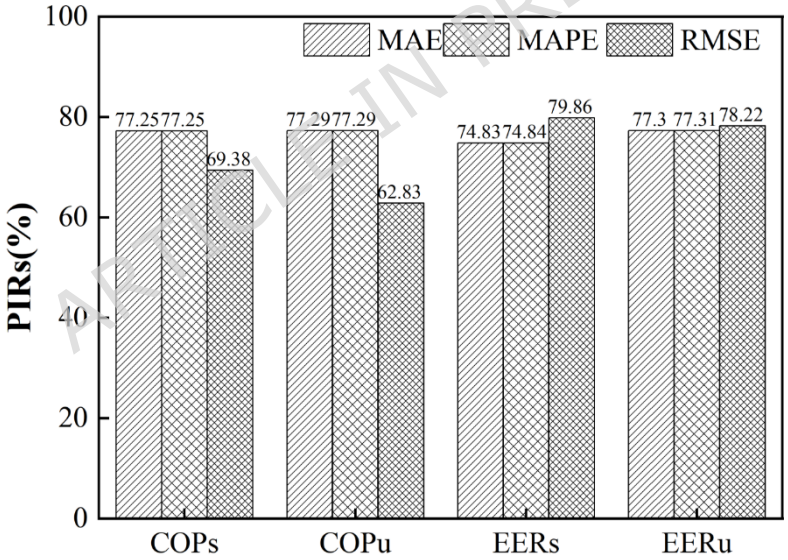

Fig. 13. Comparison of the PIR_s of the GA-BPNN and BPNN models.

4.3 Optimization results

4.3.1 Key operational variables selection results

To achieve the best energy performance of the HRGSHP system, it is essential to select and optimize the key operational parameters [36,37]. Figs. 14 and 15 present the *PPC* analysis results. The significant temperature difference between the outdoor (t) and indoor temperature setpoints leads to substantial load variations,

confirming that t is a dominant factor influencing COP_s, COP_u, EER_s, and EER_u. The outdoor humidity (d) is also strongly correlated with EER_s, but it has minimal impact on COP_s. This distinction arises from the fact that the HRGSHP system is deployed in industrial buildings with stringent humidity control requirements, where d becomes critical in governing the energy efficiency during high-temperature, high-humidity cooling periods.

The system efficiency is also strongly influenced by T_c and T_e, which are both affected by the ground-side outlet water temperature ($T_{o,g}$) and the user-side outlet water temperature ($T_{o,u}$). During the cooling season, tthe intermittent condensation heat recovery leads to a rise in T_e, significantly affecting both EER_s and EER_u. Furthermore, the user-side flow rate (G_u) is found to be a critical control variable, exhibiting strong sensitivity across all performance metrics (Figs. 14 and 15). Based on these considerations, for COP_s and COP_u, the decision variables selected are $T_{o,g}$, $T_{o,u}$, and G_u; for EER_s and EER_u, the decision variables selected are $T_{o,g}$, $T_{o,u}$, $T_{o,r}$, and G_u. Table 7 defines the feasible ranges for these variables, which are derived from operational limits and thermodynamic constraints.

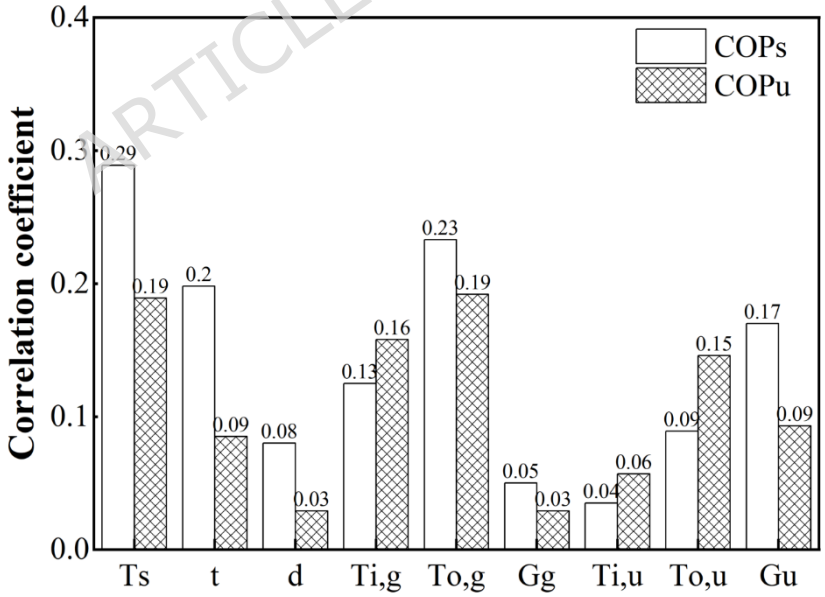

Fig. 14. *PPCs* for the *COP* and the influencing variables.

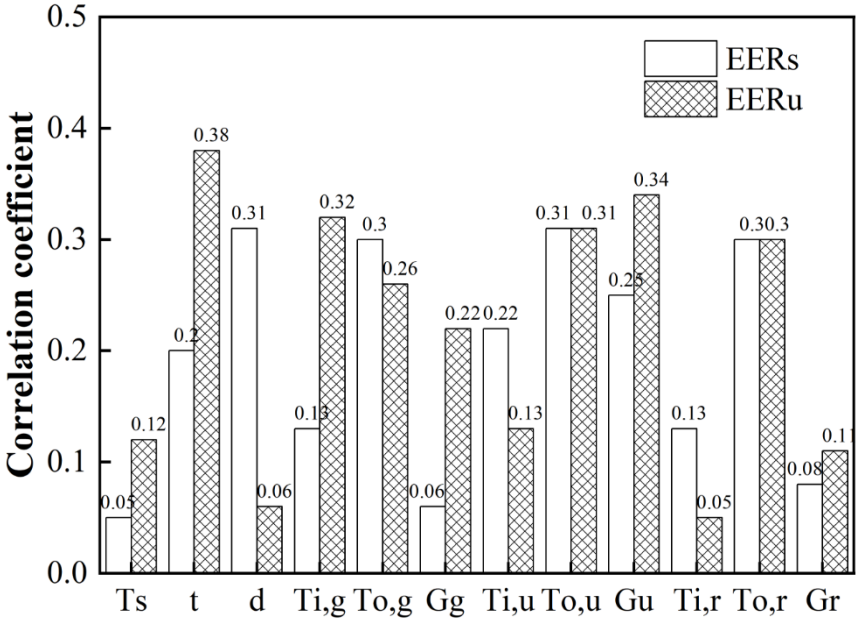

Fig. 15. *PPCs* for the *EER* and the influencing variables.

Table 7 Suitable ranges for the decision variables.

Decision variable	G_u	$T_{o,g}$	$T_{o,u}$	$T_{o,r}$
Unit	m^3/h	℃	℃	℃
Summer	[120,370]	[16-25]	[8-16]	[45-55]
Winter	[110,320]	[12-18]	[45-55]	

4.3.2 TOPSIS results

To simultaneously maximize COP_s (EER_s) and COP_u (EER_u), the TOPSIS method was here employed for selecting the operational parameter settings. The optimal results are summarized in Table 8. During the heating season, as the outdoor temperature varies, the optimal $T_{o,g}$ and $T_{o,u}$ are found to be 15.16 °C and 49.94 °C, respectively, with the optimal G_u ranging from 210 to 255 m^3/h. In the cooling season, the optimal values for $T_{o,g}$, $T_{o,u}$, and $T_{o,r}$ are 21.4 °C, 13.29 °C, and 52.69 °C, respectively, with the optimal G_u ranging from 246 to 253 m^3/h. The broader G_u range observed in the heating season is attributed to the dual-mode operation of the system in this season (cooling + hot water production), which elevates evaporator-side temperatures and requires higher flow rates to meet the user-side cooling demand.

Table 8 TOPSIS optimization results for the *COP*.

Season	Parameters	TOPSIS optimization	Pre-optimization
Winter	$T_{o,g}$ (℃)	15.16	16.16
	$T_{o,u}$ (℃)	49.67	51.16
	G_u (m^3/h)	210.82-254.94	112.77-308.39
	COP_s	3.67	2.90
	COP_u	4.17	3.75
Summer	$T_{o,g}$ (℃)	21.4	22.29
	$T_{o,u}$ (℃)	13.29	13.14
	$T_{o,r}$ (℃)	48.13	48
	G_u (m^3/h)	246.67-252.59	128.2-365.13
	EER_s	3.97	3.28
	EER_u	5.73	5.17

Fig. 16 presents the significant performance improvements obtained after optimization. The average COP_s, COP_u, EER_s, and EER_u values are increased by 27%, 11%, 21%, and 11%, respectively (Eq. (16)). These improvements are explained in Fig. 17 from a thermodynamic perspective.

In summer, T_e rises by around 2°C (state point 5 to 5'), while T_c increases only slightly (state point 4 to 4'), but the rise in T_c is smaller than that in T_e. The resulting cycle transformation reduces the compressor work (the 1–2 segment is shorter than the 1'–2' segment) and increases the cooling capacity (the area under the 1–5 segment is larger than that under the 1'–5' segment), enhancing both EER_s and EER_u. In winter, T_e rises by around 1°C (state point 5 to 5'), while T_c remains stable. This results in reduced compressor work (shorter 1–1' segment) at constant heating capacity (comparable areas under the 3–4 and 3'–4' segments), enhancing both COP_s and COP_u. Additionally, optimization of the pump frequency narrows the operating flow ranges, reducing auxiliary energy consumption and thus further improving COP_s and EER_s.

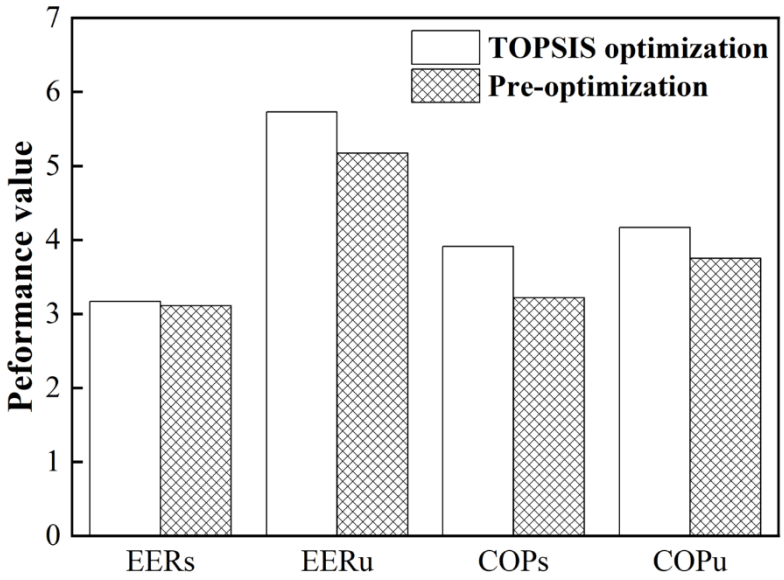

Fig. 16. Average *COP* and *EER* after and before TOPSIS optimization.

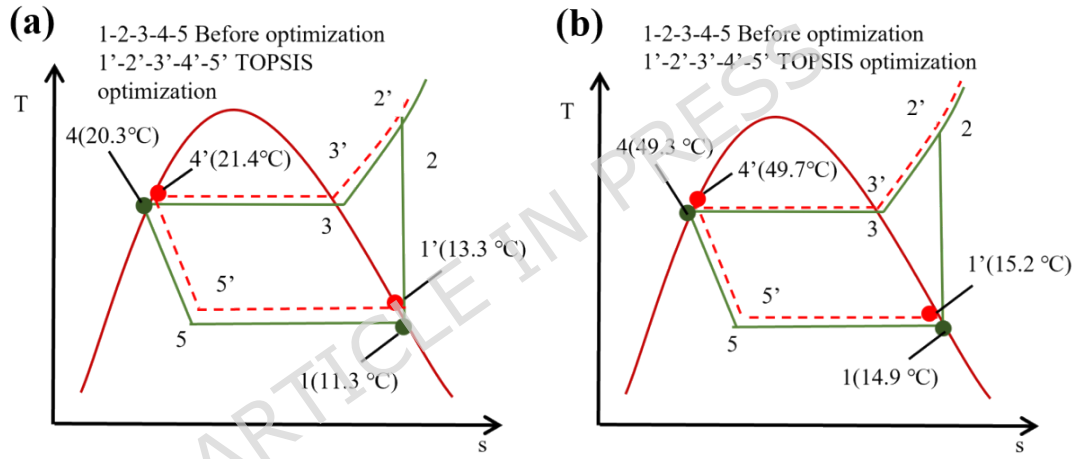

Fig. 17. Thermodynamic temperature (T)–entropy (s) diagram for the HRGSHP system before and after TOPSIS optimization: (a) summer and (b) winter.

4.3.3 Economic analysis

A simplified cost–benefit analysis was performed to evaluate the financial benefit of the proposed optimization strategy. As summarized in Table 9, optimized operation reduces electricity consumption by 17.38% (summer) and 20.98% (winter), surpassing the 12.7% reduction reported in Ref. [16]. These savings translate to cost reductions of up to 19%, which are directly attributable to the enhanced system efficiency for equivalent building load conditions. Specifically, for the GSHP system, the adopted optimization strategy results in a significant reduction in electricity consumption.

Table 9 Economic analysis before and after optimization.

Operation seasons	Load (kW)	COP_s/EER_s improvement rate	Energy saving rate	Actual electricity consumption in 2022（kWh）	Optimized power saving（kWh）	Cost saving （Yuan RMB）
Summer	1800	21%	17.38 %	651380.77	113212.27	72455.86
Winter	1500	27%	20.98 %	488334.10	102457.02	65572.49
Total					215669.29	138028.35

Note:China implements a tiered pricing system. Electricity prices in Gui Zhou range from 0.271 to 1.009, and the average is 0.64 RMB/kWh.

5 Discussion

To address the challenges of soil heat accumulation and condenser heat waste associated with conventional GSHP systems operating in cooling-dominated regions, this study proposes a novel HRGSHP configuration together with a data-driven operational optimization framework. The heat recovery concept of the proposed system can be adapted to different climatic contexts by adjusting operating modes, heat recovery capacity, and temperature control strategies according to local building load characteristics. Although the present study focuses on a cooling-dominated building, the proposed approach is also applicable to heating-dominated scenarios, particularly in buildings with sufficient domestic hot water demand or air conditioning hot water.

The GA-BPNN–based optimization framework is transferable to different building types and load profiles by retraining the data-driven models using representative operational datasets. This enables the proposed methodology to be extended beyond the specific case investigated in this study, thereby enhancing its general applicability. From an implementation perspective, the GA-BPNN–TOPSIS framework is intended to support supervisory level operation rather than direct real-time control. The optimized operational parameters can be integrated into existing building

management systems (BMS) as reference setpoints or predefined operating schedules. In practice, optimized parameter sets corresponding to different operating modes and outdoor temperature ranges can be generated offline and selected by the BMS based on current conditions. Importantly, practical operational constraints, including allowable temperature limits and flow rate boundaries, are explicitly incorporated into the optimization process to ensure feasibility and system stability.

Despite these advantages, several limitations should be acknowledged. Measurement uncertainty, ground thermal response delays, and dynamic variations in building load are not explicitly modeled in the current framework and warrant further investigation. In addition, the economic assessment presented in this study focuses primarily on operational cost savings from reduced electricity consumption. A more comprehensive life-cycle cost analysis, incorporating capital investment, electricity price variability, system degradation, and long-term financial indicators, remains an important direction for future work. Addressing these aspects would further strengthen the robustness and practical relevance of the proposed HRGSHP optimization framework.

6 Conclusion

In this study, a novel HRGSHP system was proposed and evaluated to mitigate soil heat accumulation in cooling-dominated GSHP applications while enhancing building energy performance. The actual system was monitored for approximately three years in an HSCW climate, and a model-based optimization framework was employed to improve its performance. The main conclusions are as follows:

(1) The HRGSHP system maintained long-term soil thermal stability, with only a 0.45 °C increase over three years of operation, which is significantly lower than values reported for conventional GSHP systems under comparable climatic conditions.

(2) Achieving soil thermal balance alone does not ensure high energy efficiency. Under the existing operating strategy, the average COP remained below 3, mainly due to a “small ΔT–large flow rate”

pattern, highlighting the necessity of coordinated optimization of flow rate and water temperature.

(3) During peak cooling periods, the average user-side inlet water temperature reached 8.4 °C, exceeding the design value of conventional GSHP systems and contributing to improved cooling performance.

(4) The proposed GA-BPNN model achieved approximately 90% prediction accuracy across multiple operating modes, demonstrating its robustness for performance modeling.

(5) Under optimized operating conditions, the integrated GA-BPNN–TOPSIS framework improved average COP_s, COP_u, EER_s, and EER_u by 27%, 11%, 21%, while reducing operational costs by about 19%.

Data availability

All data generated or analyzed during this study are not publicly available due to confidentiality agreements with the collaborating institution, but are available from the corresponding author on reasonable request.

References

1. Liu, Y. *et al.* Characteristics analysis and modeling of occupants' window operation behavior in hot summer and cold winter region, China. *Building and Environment* **216**, 108998 (2022).
2. Yang, X., Zhou, G., Ren, Z., Qiao, Y. & Yi, J. High-precision air conditioning load forecasting model based on improved sparrow search algorithm. *Journal of Building Engineering* **92**, 109809 (2024).
3. Abuasbeh, M., Acuña, J., Lazzarotto, A. & Palm, B. Long term performance monitoring and KPIs' evaluation of Aquifer Thermal Energy Storage system in Esker formation: Case study in

Stockholm. *Geothermics* **96**, 102166 (2021).

4. Wang, X. *et al.* A systematic review of recent air source heat pump (ASHP) systems assisted by solar thermal, photovoltaic and photovoltaic/thermal sources. *Renewable Energy* **146**, 2472–2487 (2020).
5. Self, S. J., Reddy, B. V. & Rosen, M. A. Geothermal heat pump systems: Status review and comparison with other heating options. *Applied Energy* **101**, 341–348 (2013).
6. Al-qazzaza, A. H. S., Farzaneh-Gorda, M. & Niazmand, H. Systematic analysis with comparison of a chiller plant with horizontal underground heat exchangers and cooling tower. *Journal of Building Engineering* **92**, 109665 (2024).
7. Bae, S. & Nam, Y. Economic and environmental analysis of ground source heat pump system according to operation methods. *Geothermics* **101**, 102373 (2022).
8. Esen, H., Inalli, M. & Esen, M. A techno-economic comparison of ground-coupled and air-coupled heat pump system for space cooling. *Building and Environment* **42**, 1955–1965 (2007).
9. Xu, L., Pu, L., Zhang, S. & Li, Y. Hybrid ground source heat pump system for overcoming soil thermal imbalance: A review. *Sustainable Energy Technologies and Assessments* **44**, 101098 (2021).

10. Qian, H. & Wang, Y. Modeling the interactions between the performance of ground source heat pumps and soil temperature variations. *Energy for Sustainable Development* **23**, 115–121 (2014).

11. Lee, J. S., Song, K. S., Ahn, J. H. & Kim, Y. Comparison on the transient cooling performances of hybrid ground-source heat pumps with various flow loop configurations. *Energy* **82**, 678–685 (2015).

12. Man, Y., Yang, H. & Wang, J. Study on hybrid ground-coupled heat pump system for air-conditioning in hot-weather areas like Hong Kong. *Applied Energy* **87**, 2826–2833 (2010).

13. Yi, M., Hongxing, Y. & Zhaohong, F. Study on hybrid ground-coupled heat pump systems. *Energy and Buildings* **40**, 2028–2036 (2008).

14. Wu, J. *et al.* Intelligent Diagnosis Method of Data Center Precision Air Conditioning Fault Based on Knowledge Graph. *Electronics* **12**, (2023).

15. Zhao, Z., Shen, R., Feng, W., Zhang, Y. & Zhang, Y. Soil Thermal Balance Analysis for a Ground Source Heat Pump System in a Hot-Summer and Cold-Winter Region. *Energies* **11**, 1206 (2018).

16. Zhang, S. *et al.* Field testing and performance analyses of ground source heat pump systems for residential applications in Hot

Summer and Cold Winter area in China. *Energy and Buildings* **133**, 615–627 (2016).

17. Chiam, Z., Papas, I., Easwaran, A., Alonso, C. & Estibals, B. Holistic optimization of the operation of a GCHP system: A case study on the ADREAM building in Toulouse, France. *Applied Energy* **321**, 119377 (2022).
18. Montagud, C., Corberán, J. M. & Montero, Á. In situ optimization methodology for the water circulation pumps frequency of ground source heat pump systems. *Energy and Buildings* **68**, 42–53 (2014).
19. Park, H., Lee, J. S., Kim, W. & Kim, Y. Performance optimization of a hybrid ground source heat pump with the parallel configuration of a ground heat exchanger and a supplemental heat rejecter in the cooling mode. *International Journal of Refrigeration* **35**, 1537–1546 (2012).
20. Sivasakthivel, T., Murugesan, K. & Thomas, H. R. Optimization of operating parameters of ground source heat pump system for space heating and cooling by Taguchi method and utility concept. *Applied Energy* **116**, 76–85 (2014).
21. Lu, S., Li, Q., Bai, L. & Wang, R. Performance predictions of ground source heat pump system based on random forest and back propagation neural network models. *Energy Conversion and*

Management **197**, 111864 (2019).

22. Sun, W., Hu, P., Lei, F., Zhu, N. & Jiang, Z. Case study of performance evaluation of ground source heat pump system based on ANN and ANFIS models. *Applied Thermal Engineering* **87**, 586–594 (2015).

23. Zhang, X., Wang, E., Liu, L. & Qi, C. Machine learning-based performance prediction for ground source heat pump systems. *Geothermics* **105**, 102509 (2022).

24. Karami, A. Power system transient stability margin estimation using neural networks. *International Journal of Electrical Power & Energy Systems* **33**, 983–991 (2011).

25. Wang, Z. & Srinivasan, R. S. A review of artificial intelligence based building energy use prediction: Contrasting the capabilities of single and ensemble prediction models. *Renewable and Sustainable Energy Reviews* **75**, 796–808 (2017).

26. Yan, L. *et al.* The performance prediction of ground source heat pump system based on monitoring data and data mining technology. *Energy and Buildings* **127**, 1085–1095 (2016).

27. Zhou, S., Cui, W., Zhao, S. & Zhu, S. Operation analysis and performance prediction for a GSHP system compounded with domestic hot water (DHW) system. *Energy and Buildings* **119**, 153–163 (2016).

28. Hu, R., Li, X., Liang, J., Wang, H. & Liu, G. Field study on cooling performance of a heat recovery ground source heat pump system coupled with thermally activated building systems (TABSs). *Energy Conversion and Management* **262**, 115678 (2022).

29. Chen, H. & Lee, W. L. Combined space cooling and water heating system for Hong Kong residences. *Energy and Buildings* **42**, 243–250 (2010).

30. Luo, J., Xue, W., Hu, T., Xiang, W. & Rohn, J. Thermo-economic analysis of borehole heat exchangers (BHE) grouted using drilling cuttings in a dolomite area. *Applied Thermal Engineering* **150**, 305–315 (2019).

31. Zhang, S., Zhang, L. & Zhang, X. Performance evaluation of existed ground source heat pump systems in buildings using auxiliary energy efficiency index: Cases study in Jiangsu, China. *Energy and Buildings* **147**, 90–100 (2017).

32. Lee, S. H. & Chen, W. A comparative study of uncertainty propagation methods for black-box-type problems. *Struct Multidisc Optim* **37**, 239–253 (2009).

33. Adams, B. M. *et al.* Dakota, A Multilevel Parallel Object-Oriented Framework for Design Optimization, Parameter Estimation, Uncertainty Quantification, and Sensitivity Analysis: Version 6.13 User's Manual.

34. Spitz, C., Mora, L., Wurtz, E. & Jay, A. Practical application of uncertainty analysis and sensitivity analysis on an experimental house. *Energy and Buildings* **55**, 459–470 (2012).

35. Ertesvåg, I. S. Uncertainties in heat-pump coefficient of performance (COP) and exergy efficiency based on standardized testing. *Energy and Buildings* **43**, 1937–1946 (2011).

36. Gong, X., Xia, L., Ma, Z., Chen, G. & Wei, L. Investigation on the optimal cooling tower input capacity of a cooling tower assisted ground source heat pump system. *Energy and Buildings* **174**, 239–253 (2018).

37. Noorollahi, Y., Saeidi, R., Mohammadi, M., Amiri, A. & Hosseinzadeh, M. The effects of ground heat exchanger parameters changes on geothermal heat pump performance – A review. *Applied Thermal Engineering* **129**, 1645–1658 (2018).

38. Wang, C. *et al.* Research on the operation features and optimization methods of heat pumps coupled with mid-deep borehole heat exchangers: On-site measurements and comparative study. *Energy and Buildings* **328**, 115239 (2025).

39. Ren, C. *et al.* Optimal parameters selection for BP neural network based on particle swarm optimization: A case study of wind speed forecasting. *Knowledge-Based Systems* **56**, 226–239 (2014).

40. Kumar, R., Kumar, P. & Kumar, Y. Time Series Data Prediction

using IoT and Machine Learning Technique. *Procedia Computer Science* **167**, 373–381 (2020).

41. Zhang, L. & Wang, L. Optimization of site investigation program for reliability assessment of undrained slope using Spearman rank correlation coefficient. *Computers and Geotechnics* **155**, 105208 (2023).

42. Hong, H., Liu, J. & Zhu, A.-X. Modeling landslide susceptibility using LogitBoost alternating decision trees and forest by penalizing attributes with the bagging ensemble. *Science of The Total Environment* **718**, 137231 (2020).

43. Ding, S., Li, R. & Guo, J. An entropy-based TOPSIS and optimized grey prediction model for spatiotemporal analysis in strategic emerging industry. *Expert Systems with Applications* **213**, 119169 (2023).

44. *Renewable Energy Building Application Engineering Evaluation Standard*. vol. GB/T50801 (Inspection and Quarantine of the People's Republic of China, 2013).

45. Aslay, S. E. Building energy prediction model with AI-based PSO-ANN approach integrating architectural and HVAC processes. *Building and Environment* **282**, 113305 (2025).

Acknowledgments

The work described in this paper was supported by all authors. Special thanks to Guizhou China Tobacco Industry Co., Ltd., Tongren

Cigarette Factory, for its data assistance during the preparation of this manuscript.

Author contributions

Ying Cui: Conception and design of study, Methodology, Software–MATLAB, Writing–Original draft preparation, Data curation–Acquisition, analysis, and interpretation of data, Writing–Reviewing and editing, Validation, Supervision, Visualization. **Wen Tong Chong**: Writing–Reviewing, Supervision. **Mahendra Varman**: Writing–Reviewing, Supervision. **Xinru Wang**: Reviewing, Writing–Reviewing, Supervision. **Taocheng Wan**: Software. **Yun Deng**: Data curation–Provide the study data, Writing—Reviewing. **Song Pan**: Writing-Reviewing.

Funding

This research did not receive any specific grant from funding agencies in the public, commercial, or not-for-profit sectors.

Declarations

Competing Interest

The authors declare that they have no known competing financial interests or personal relationships that could have appeared to influence the work reported in this paper.